

Investigation of Fe-Ag and Ag-Fe Interfaces in Ag/⁵⁷Fe/Ag/[W/Si]₁₀ Multilayers Using Nuclear Resonance Scattering under X-ray Standing Wave Conditions

Manisha Priyadarsini¹, Sharanjeet Singh¹, Ilya Sergeev², Olaf Leupold², Ajay Gupta³, Dileep Kumar^{1*}

¹UGC-DAE Consortium for Scientific Research, Khandwa Road, Indore -452001, India

²Deutsches Elektronen-Synchrotron DESY, Hamburg 22607, Germany

³Department of Physics, University of Petroleum and Energy Studies, Bidholi Campus, Dehradun 248007, India

*Corresponding author: dkumar@csr.res.in

Abstract

Understanding the interfaces of layered nanostructures is key to optimizing their structural and magnetic properties for the desired functionality. In the present work, the two interfaces of a few nm thick Fe layer in Ag/⁵⁷Fe/Ag trilayer are studied with a depth resolution of a fraction of a nanometer using x-ray standing waves (XSWs) generated by an underlying [W/Si]₁₀ multilayer (MLT) at an x-ray incident angle around the Bragg peak of the MLT. Interface selectivity in Ag/⁵⁷Fe/Ag was achieved by moving XSW antinodes across the interfaces by optimizing suitable incident angles and performing depth-resolved nuclear resonance scattering (NRS) and X-ray fluorescence (XRF) measurements for magnetic and structural properties. The combined analysis revealed that the rms roughness of ⁵⁷Fe-on-Ag and Ag-on-⁵⁷Fe interfaces are not equal. The roughness of the ⁵⁷Fe-on-Ag interface is 10 Å, while that of the Ag-on-⁵⁷Fe interface is 6 Å. n⁵⁷Fe isotope sensitive NRS revealed that hyperfine field (HFF) at both interfaces of ⁵⁷Fe-on-Ag and Ag-on-⁵⁷Fe interfaces are distinct which is consistent with the difference in interface roughnesses measured as root mean square (RMS) roughness. Thermal annealing induces ⁵⁷Fe diffusion into the Ag layer, and annealing at 325 °C transforms the sample into a paramagnetic state. This behavior is attributed to forming ⁵⁷Fe nanoparticles within the Ag matrix, exhibiting a paramagnetic nature. These findings provide deep insights into interface properties crucial for developing advanced nanostructures and spintronic devices.

Keywords: X-ray standing wave, hyperfine field, interface, diffusion, multilayer etc.

INTRODUCTION

Magnetic multilayers have revolutionized the fields of spintronics and nanotechnology owing to their exceptional magnetoresistance, tunable anisotropy, and interface-driven phenomena. Interfaces play a pivotal role in shaping the magnetic properties of multilayer nanostructures, influencing phenomena such as giant magnetoresistance (GMR), interlayer coupling (ILC), and perpendicular magnetic anisotropy (PMA). Consequently, understanding and optimizing interface structures are essential for enhancing the performance and reliability of devices like magnetic random-access memory (MRAM), sensors, and spintronic components.

Fe/Ag systems stand out among magnetic multilayers due to their unique magnetic behaviours and technological relevance. These systems exhibit intriguing phenomena, such as GMR [1–3], PMA [4], and ILC [5–7], at specific Fe layer thicknesses. For example, silver (Ag), as a non-magnetic spacer, enhances the magnetic coupling between iron (Fe) layers, improving GMR effects. The magnetic behavior of these multilayers is highly sensitive to interface quality, with asymmetric diffusion and intermixing at Fe-on-Ag and Ag-on-Fe interfaces playing a critical role. Fe/Ag is a system with a significant positive heat of mixing ($\Delta H_{\text{solid}} = 42 \text{ kJ/mol}$; $\Delta H_{\text{liq}} = 28 \text{ kJ/mol}$) both in solid and liquid phases [8]. Extensive studies have been done in the literature to see possible intermixing in this system using non-equilibrium techniques like heavy ion irradiation [9]. Schurrer *et al.* used a monolayer of ^{57}Fe as a Mössbauer probe of either the Fe-on-Ag or Ag-on-Fe interface in two different samples, have demonstrated differences in average magnetic moments at these interfaces due to asymmetric diffusion [10]. While there have been extensive studies on Fe/Ag systems, much of the research has focused on magnetoresistance or bulk properties, leaving key questions about the structural and magnetic asymmetries at the interfaces largely unexplored [11]. Also, the mixing at the interface and the origin of interlayer coupling are not fully understood. Many techniques [12,13] have been used to characterize the interfaces in such multilayers. Still, it lacks depth resolution to probe individual interfaces' structure and magnetic configuration or may not be able to probe true interfaces.

Additionally, in a multilayer system, as the number of bilayers increases, the interface roughness of the successive layers can vary unpredictably. Properties of such multilayers have an average effect over many interfaces, making the interpretation of the data difficult. The need for simultaneous, independent characterization of both interfaces in a single sample remains unmet, leaving ambiguities in the origins of ILC, PMA, and other phenomena [14,15]. To date, the direct measurement of both interfaces (A-on-B and B-on-A) independently in the same

multilayered sample remains unachievable. These questions demand innovative experimental approaches with atomic-scale resolution to characterize interface-specific phenomena.

To solve the existing ambiguities, it is necessary that: i) both interfaces should be studied independently in identical conditions (in the same sample) to correlate with existing properties such as GMR, PMA, and ILC in the sample; ii) trilayer film structure has to be studied to avoid the effect of averaging over large inequivalent interfaces in a multilayers structure. To meet these requirements, Ag/⁵⁷Fe/Ag trilayers stand out as model systems for exploring the complex interplay of structural and magnetic properties at nanoscale interfaces. Studying such systems is crucial for understanding interface physics and advancing technologies like high-density storage, spin valves, and tunneling magnetoresistance TMR-based devices. The availability of high-brilliance synchrotron radiation has recently opened new avenues for applying the nuclear resonance scattering (NRS) method in ultra-thin films [16–22]. Novel features such as high sensitivity and isotope selectivity of this technique enable us to characterize subtle variations in the magnetic structure [23,24], such as orientation and magnitude of the hyperfine field at both interfaces by using a layer of the nuclear isotope, such as ⁵⁷Fe in place of natural Fe [21,25–27]. In addition to these depth-resolved measurements, X-ray standing wave conditions will allow us to resolve the magnetic structure of both interfaces independently in the same sample [8,18,28–34].

In the present work, we investigate the Ag/⁵⁷Fe/Ag trilayer system, utilizing the unique advantages of synchrotron-based NRS under XSW conditions, providing a comprehensive depth-selective analysis of the structural and magnetic properties at both interfaces. Resolving the magnetic and structural properties at the Fe-on-Ag and Ag-on-Fe interfaces aims to uncover the interplay between interface structure and magnetic properties. These findings are expected to contribute to developing next-generation magnetic nanotechnologies, including high-density storage and spintronic devices, and provide a general framework for exploring similar multilayer systems with complex interface-driven effects.

EXPERIMENTAL

The multilayer structure studied here consists of [W (20 Å)/Si (30 Å)]₁₀/Si (9 Å)/Ag (25 Å)/⁵⁷Fe (40 Å)/Ag (25 Å)/Si (120 Å), as depicted in Fig. 2(a). The structure was fabricated using ion-beam sputtering in a vacuum chamber maintained at a base pressure of 1×10^{-7} mbar. This deposition technique is well-suited for achieving smooth and well-defined interfaces, critical for enhancing reflectivity in X-ray standing wave (XSW) experiments. The W/Si

multilayer, consisting of 10 bilayers, serves as a substrate to generate XSWs, providing a platform for studying the subsequent Ag/⁵⁷Fe/Ag trilayer.

The Ag/⁵⁷Fe/Ag structure was engineered such that the antinodes of the XSW selectively overlap with the two interfaces (Ag-on-⁵⁷Fe and ⁵⁷Fe-on-Ag) at specific incident angles. Theoretical simulations of fluorescence and reflectivity were performed to optimize the multilayer's thickness, ensuring that the standing wave antinodes intersect the desired interfaces. By varying the angle of incidence of X-rays near the Bragg peak of the W/Si multilayer, the position of the antinodes was shifted across the thickness of the trilayer.

Depth-resolved elemental profiles were obtained using X-ray fluorescence (XRF) as the XSW antinodes swept across the interfaces. The fluorescence spectrum was recorded with an Amptek XR-100T/CR PIN diode detector featuring an energy resolution of 250 eV. To investigate the effects of thermal annealing, fluorescence measurements were also conducted after isochronal annealing at 225 °C and 325 °C for one hour each under a vacuum of 1×10^{-8} mbar. This annealing process enabled the study of Fe intermixing and structural changes at the interfaces.

Conversion electron Mössbauer spectroscopy (CEMS) and nuclear resonance scattering (NRS) measurements were performed in pristine and annealed states to characterize further the intermixed region's volume fraction and hyperfine field. The NRS measurements were conducted at the nuclear resonance beamline P01 at PETRA III, DESY, Germany, using energy 14.4 keV. The resonance signal of the ⁵⁷Fe layer was enhanced by the standing waves generated via Bragg reflection from the W/Si multilayer. Additionally, the magnetic properties of the Fe films were evaluated using the magneto-optic Kerr effect (MOKE). Room-temperature magnetization curves were measured in longitudinal geometry with an applied magnetic field of up to 300 Oe. Combining these complementary techniques provided a comprehensive understanding of the magnetic and structural evolution of the multilayer system under thermal treatment.

THEORETICAL BACKGROUND:

XSW techniques have become a crucial tool for depth-resolved measurements in distinct processes such as probing the interface structure in the FM/OSC bilayer, magnetism in buried layers, atomic migration, interface intermixing, and annealing-induced changes at the interface [35–38]. In this study, the theoretical framework of XSW is employed to probe the interfacial asymmetries in an Ag/⁵⁷Fe/Ag trilayer system. The XSW is generated within the multilayer

structure by the coherent scattering of monochromatic X-rays, leading to an intensity modulation at specific depths [18]. If we consider a multilayer structure, the intensity of the secondary radiation ($A_f(z)$) created at depth z is proportional to the square module of the total X-ray field amplitude $E(z)$ at depth z is given by,

$$A_f(z) \sim N_F(z) |E(z)|^2 = N_F(z) |E^t(z) + E^r(z)|^2 \quad (1)$$

Where, $E^t(z)$ and $E^r(z)$ are the amplitudes of incident and reflected waves, $N_F(z)$ is the volume density of the fluorescent atoms. The positions of the standing wave antinodes can be shifted by slightly varying the incidence angle of X-rays [32,35,39]. The reflectance of an ultrathin layer positioned z away from a multilayer, I_R , in the simplest scenario, is determined by

$$I_R = |r E(z)^2|^2, \quad (2)$$

where r is the reflectivity amplitude from the same layer in a vacuum. It follows from (2) that the reflectivity from an ultrathin layer is enhanced by the fourth power of the standing wave amplitude $E(z)$, which is true in the general case. Therefore, standing waves have an even greater impact on reflectivity than secondary radiations. The problem of how to extract the contribution from a selected layer in the total reflectivity intensity can be resolved by the resonant energy or time reflectivity dependence. So, resonant reflectivity has a great potential for depth-selective investigations.

Nuclear resonant reflectivity from the films containing Mossbauer isotopes is normally measured with synchrotron radiation in the time domain. Reflectivity amplitudes in the energy $R(\omega)$ and time $R(t)$ domains are connected by the Fourier transform.

$$R(t) = \frac{1}{2\pi} \int_{-\infty}^{\infty} R(\omega) e^{-i\omega t} d\omega \quad (3)$$

So, for each grazing angle, the time spectrum of the nuclear resonant reflectivity can be calculated,

$$I_{nucl}(t, \theta) = A |R(t, \theta)|^2 \quad (4)$$

(a normalization factor A is determined by the total amount of resonant quanta in the bunches of the synchrotron radiation). When equation (2) is integrated over the delay time for each, the delayed nuclear resonant reflectivity curve is obtained:

$$I_{nucl}(\theta) = A \int_{-\infty}^{\infty} |R(t, \theta)|^2 dt \quad (5)$$

This equation characterizes the depth position of the resonant nuclei. It may be noted that the nuclear resonance part of the signal, proportional to the fourth power of the standing wave amplitude, offers significantly greater sensitivity than other XSW-based techniques, such as

X-ray fluorescence. This enhanced sensitivity is critical in resolving this study's interfacial asymmetries and magnetic transitions.

RESULTS

The multilayer structure depicted in Fig. 1(a) illustrates the formation of nodes and antinodes at specific depth positions. The sample's X-ray reflectivity (XRR) and the corresponding Scattering length density (SLD) versus thicknesses are shown in Fig. 1(b) and (c), respectively. The XRR profile of the multilayer, measured in its as-prepared state, presents the reflected intensity as a function of the scattering vector, $q = 4\pi \sin(\theta/\lambda)$, where θ is the angle of incidence and λ is the wavelength of incident X-ray. The distinct Bragg peak in the reflectivity indicates the bilayer periodicity of the underlying W/Si multilayer.

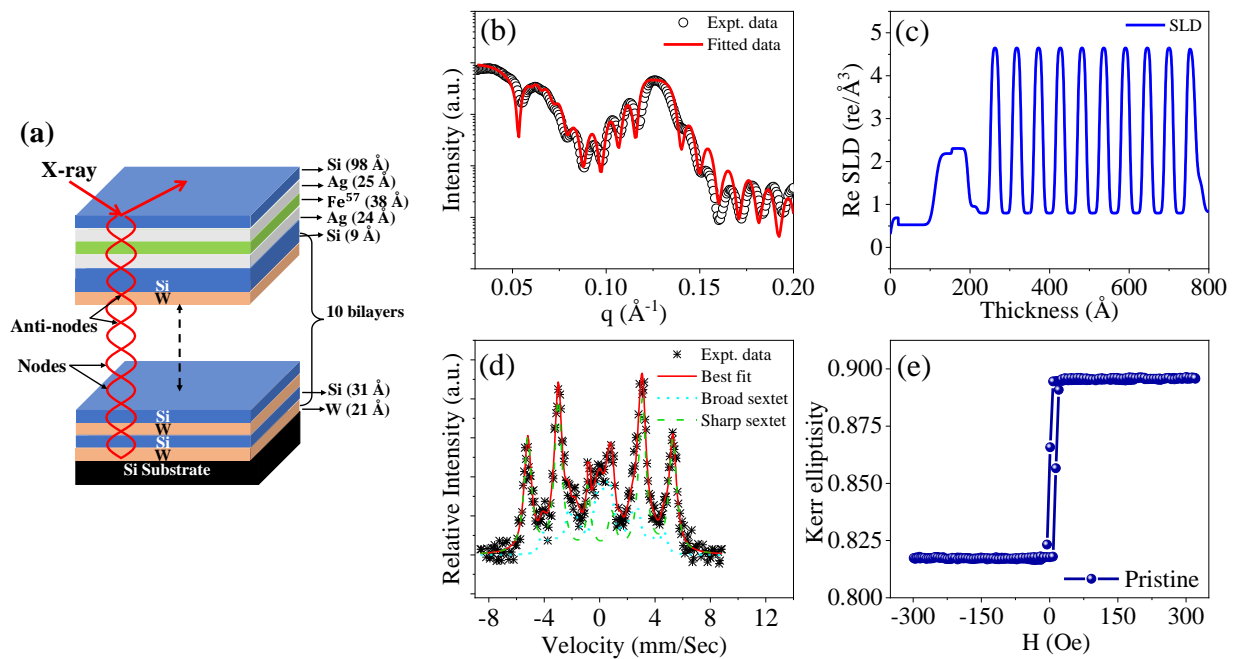


Figure 1. Schematic of the complete multilayer structure (a). The XRR plot (b) and the corresponding electron scattering density profile (c) for the as-prepared sample. (d) Depicts the CEMS spectra of the sample along with fitting, and (e) represents the hysteresis loop of the sample in an as-prepared state. The red lines represent the fitting to the experimental data (scattered curves).

The X-ray reflectivity of the structure is fitted using the GenX software [40]. The scattered curve gives the experimental data, and the continuous curve shows the fitted reflectivity data. The best fit to the data is obtained by considering the fitting parameters such as the sample's thickness, density, and roughness. It is clear that the reflectivity of the complete structure is dominated by that of the underlying W/Si multilayer. Therefore, it is not possible to get the thickness and roughness of the individual Ag and Fe layers very reliably. However, the total film thickness can be obtained from the period of Kiessig oscillations, and information such as

bilayer periodicity and average interface roughness of the underlying W/Si multilayer can be obtained by the position and the intensity of the Bragg peak. From the fitting of XRR data, the multilayer structure is obtained as [W (21 Å)/Si (31 Å)] \times 10/Si (9 Å)/Ag (24 Å)/ ^{57}Fe (38 Å)/Ag (25 Å)/Si (98 Å), and these thicknesses are shown in the sample structure in Fig. 1(a).

The samples were investigated using CEMS AND MOKE measurements to get information about the hyperfine field and magnetism at the interfaces and bulk part of the Fe layers. Fig.1 (d) shows the CEMS spectra of the pristine sample. The spectra show a sextet structure. The CEMS spectra have been fitted using two sextet structures: broad for the interfacial region and sharp for the bulk ^{57}Fe layer. Fig.1(e) shows the hysteresis loop obtained from MOKE measurements for the pristine sample. The plot shows that the loop is square shaped with $H_c \sim 7$ Oe and $M_r/M_s \sim 0.8$.

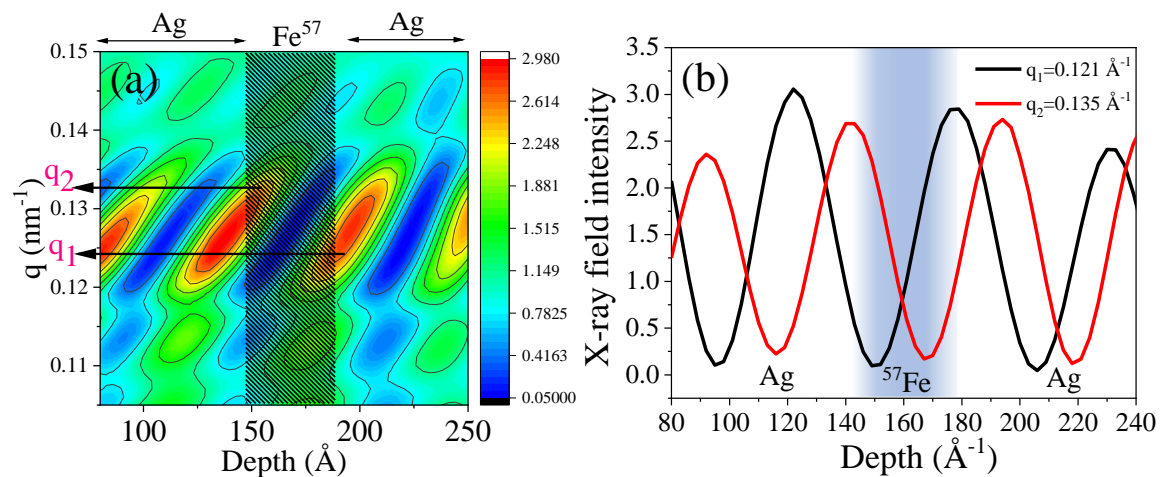


Figure. 2 (a) Calculated X-ray field intensity profile produced by the W/Si multilayer structure. (b) represents the variation of standing wave field intensity along the ^{57}Fe layer at $q_1 = 0.121 \text{ \AA}^{-1}$ (TE₁ mode), $q_2 = 0.132 \text{ \AA}^{-1}$ (TE₂ mode).

The XSW contour plot was simulated using parameters obtained from the fitting of the XRR data. Fig. 2 (a) gives the contour plot for the X-ray intensity distribution profile inside the Ag/ ^{57}Fe /Ag trilayer as a function of q . The X-ray standing wave is formed by the W/Si multilayer structure, which acts as a substrate for studying Ag/ ^{57}Fe /Ag trilayer structure. When the X-rays are allowed to fall on the system at an angle corresponding to the Bragg peak of the W/Si multilayer, standing waves are generated in the system, which extend beyond the W/Si multilayer and into the Ag/ ^{57}Fe /Ag trilayer. The positions of the antinodes can be varied by varying the angle of incidence; as the angle of incidence is varied across the width of the

multilayer Bragg peak, the position of the antinode moves over the bilayer thickness. The shaded region shows the position of the ^{57}Fe layer. The 2nd antinode ($q \sim 0.132 \text{ \AA}^{-1}$) crosses through the top interface, i.e., the Ag-on-Fe layer, whereas the bottom interface, i.e., Fe-on-Ag, overlaps with the third antinode at $q \sim 0.121 \text{ \AA}^{-1}$. Figure 2(b) shows the XSW field intensity variations at the two interfaces corresponding to two distinct q values. A significant contrast in the X-ray field intensity is observed at the interfaces of the ^{57}Fe layer, attributed to the strong intensity difference between the W and Si layers. These conditions enable precise depth-selective measurements to extract detailed information from both interfaces.

The contour plot is simulated based on parameters obtained through XRR fitting to visualize the X-ray field intensity distribution. However, XRR alone cannot provide accurate thickness and roughness values, as the W/Si multilayer structure predominantly influences it. To address this limitation, XRF data was measured. Fig. 3 (a) denotes the normalized Fe fluorescence data of the sample corresponding to the first Bragg peak in the XRR. Two separate peaks at $q=0.121 \text{ \AA}^{-1}$ and 0.132 \AA^{-1} from the single Fe layer are observed around the Bragg condition. Two peaks in fluorescence correspond to these two q values; hence, we have information from both interfaces at these q values.

The origin of these two fluorescence peaks can be understood in terms of the variation of the X-ray standing wave intensity inside the multilayer as a function of the incident angle, as shown in Fig. 2 (a). For $q = 0.121 \text{ \AA}^{-1}$, the r^{th} antinode partly overlaps with the Fe-on-Ag interface of the Fe layer, giving rise to the high-intensity peak in the fluorescence. With increasing q , this antinode moves out of the Fe layer, thus decreasing the fluorescence intensity. However, as the q increases, $(r+1)^{\text{th}}$ antinode moves inside and partially overlaps with the Ag-on-Fe interface, giving rise to the next peak at $q = 0.132 \text{ \AA}^{-1}$ [Fig. 2 (b)].

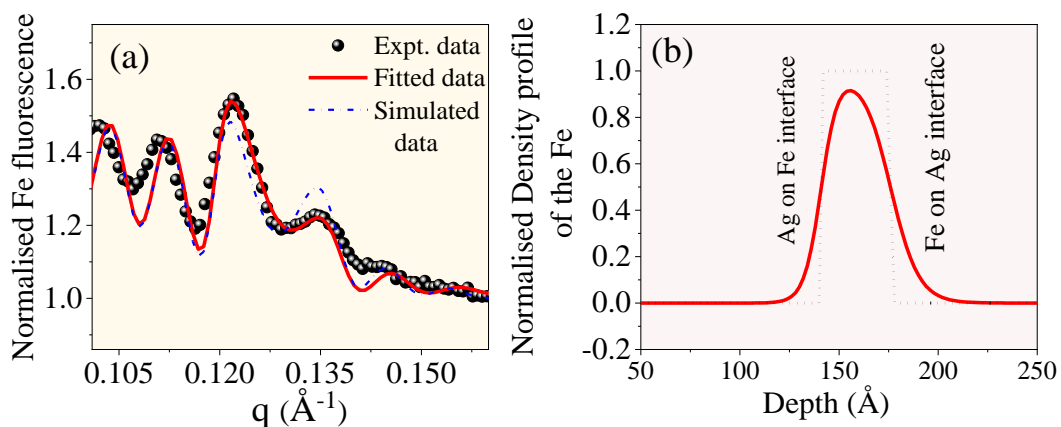


Figure. 3 Fe Fluorescence of the multilayer (a), black spheres represent the experimental data obtained, and the red line represents the best fit to the experimental data. The normalized density profile of Fe along the depth (b).

Therefore, these two peaks have information about the top (Ag-on-Fe) and bottom (Fe-on-Ag) interface of the Fe layer. To obtain quantitative information about the roughness of two interfaces of Fe, the fluorescence data fitting has been done and is shown as a continuous line in Fig. 3 (a). The best fit to the experimental data is obtained with a roughness of the Fe-on-Ag interface as $10 \pm 1.0 \text{ \AA}$ and that of Ag-on-Fe as $6 \pm 1.0 \text{ \AA}$. For comparison, the simulated fluorescence for Fe-on-Ag interface = Ag-on-Fe interface = 8 \AA is also shown with the dotted curve in Fig. 3 (a). The normalized density profile obtained from the XRF fitting is shown in Fig. 3(b). This shows two different density profiles at the two interfaces.

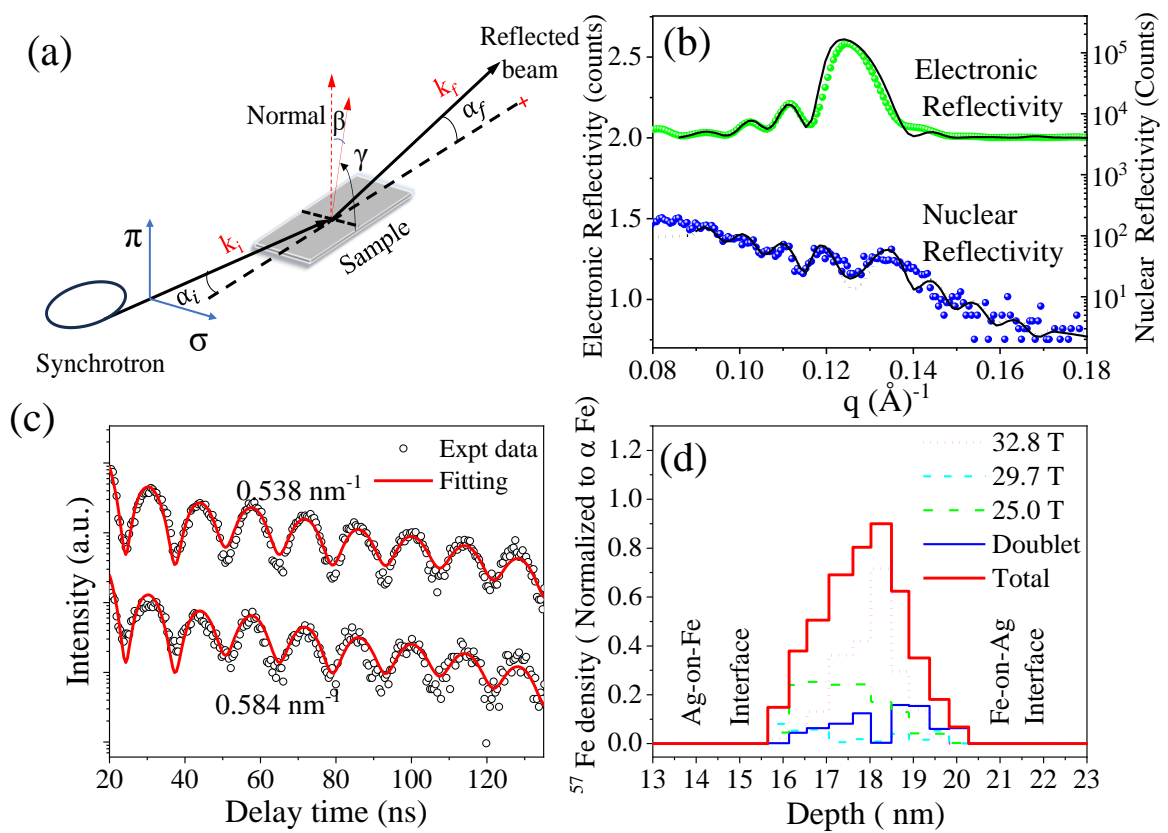


Figure 3. (a) Shows the schematic of the GINRS measurements. (b) Represents the electronic and the nuclear reflectivity profile, and (c) denotes the time spectra of the sample. (d) denotes the depth distribution of the ^{57}Fe nuclei with the contribution of different hyperfine fields obtained from the simultaneous fitting of NRR and time spectra.

The X-ray intensity contrast between W and Si layers enables precise depth-selective analysis of ^{57}Fe interfaces using the Synchrotron-based GINRS measurements. Nuclear resonance reflectivity (NRR) was performed on the samples. Figure. 3 (a) shows the schematics for the GINRS measurements. Here, α_i and α_f stand for the incidence and reflected angles of the synchrotron beam, while k_i and k_f represent the incident and reflected wave vectors. The

combined plot for fitted electronic reflectivity and NRR is shown in Fig. 3 (b). The nominal multilayer structure is decided by simulating (theoretically) the fluorescence and reflectivity of the multilayer. This was done by adjusting the thickness of the Si layer (just below the bottom Ag layer), thereby controlling the position of the Ag/⁵⁷Fe and ⁵⁷Fe/Ag interfaces relative to the standing wave pattern generated by the underlying W/Si mirror. The two NRR peaks of almost equal intensity were found, and each peak had information about the separate interface of Fe (⁵⁷Fe/Ag and Ag/⁵⁷Fe). Compared to XRF, which shows two peaks of differing intensity due to only electronic contribution (f_e), NRR exhibits peaks with equal intensity because the scattering amplitude (f) includes both resonant nuclear contribution (f_n) in addition to non-resonant electronic (f_e) contribution (i.e., $f = f_e + f_n$). Further, to obtain the interface-weighted magnetic information from the ⁵⁷Fe layer, we performed the NRS time spectra on the sample. The time spectra of the sample have been taken at these two angles ($q = 0.121 \text{ \AA}^{-1}$ and 0.132 \AA^{-1}), shown in Fig. 3 (c). To get the quantitative information, the times spectra were fitted using the REFTIM software [41].

Effect of thermal annealing:

The sample was annealed at various temperatures to investigate the thermal effects on its magnetism and hyperfine field. Fig. 4(a) and (b) show the representative XRR as a function of the scattering vector for the samples annealed at 225 °C and 325 °C. The XRR data is fitted considering different roughness values at the two interfaces.

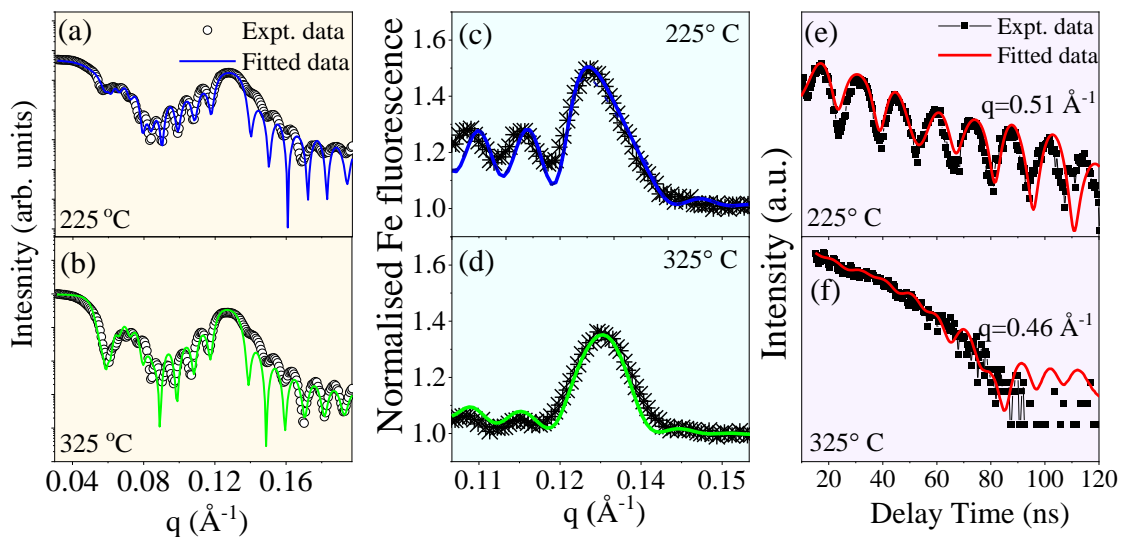


Figure 4. (a) and (b) Show the Reflectivity, (c) and (d) represent the normalized Fe fluorescence, and (e) and (f) represent the NRS time spectra for the samples annealed at 225 °C and 325 °C. The scattered curve represents the experimental data, and the continuous curve represents the best fit.

The normalized Fe fluorescence spectra are measured at both the temperatures shown in Fig. 4(c) and (d) as a function of the momentum transfer vector, q . At 225 °C, two fluorescence peaks are still visible, as in the pristine sample, whereas after annealing at 325 °C, only a single fluorescence peak is observed. The fitted time spectra of the annealed samples are shown in Fig. 4 (e) and (f).

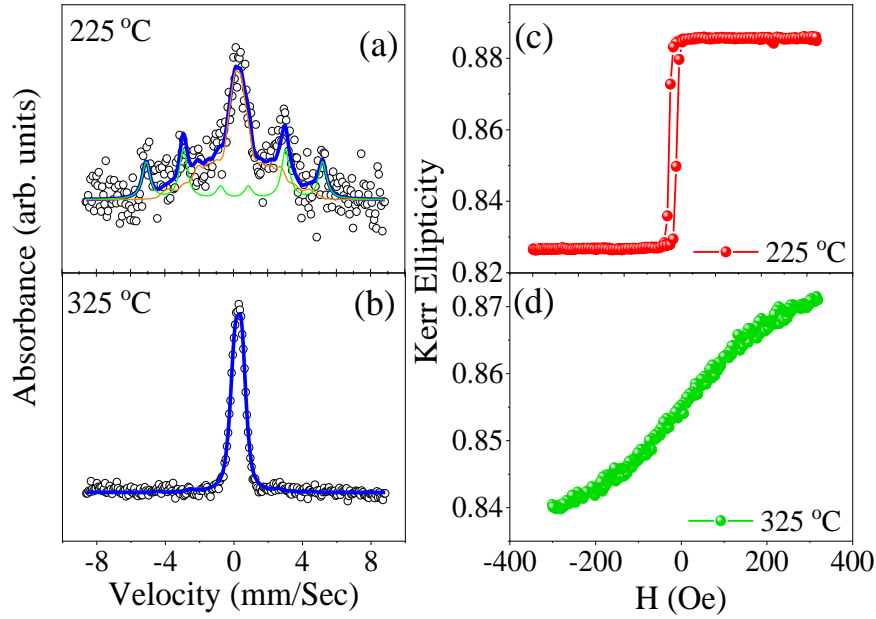


Figure 5. (a) and (b) Show the normalized Fe fluorescence, (c) and (d) represent the CEMS spectra, and (e) and (f) represent the hysteresis loops for the samples annealed at 225 °C and 325 °C.

Table 1: Fitting parameters obtained from the CEMS spectrum of the as-prepared sample. S.S. represents sharp sextet, B.S. represents broad sextet, BHF is the magnetic hyperfine, and RAS/B is the relative area of sharp to broad sextet.

| Sample | BHF _{s.s.} (T) | BHF _{B.s.} (T) | IS.S. (mm/s) | I B.S. (mm/s) | RA _{S/B} |
|----------|----------------------------|----------------------------|-----------------|------------------|-------------------|
| Pristine | 32.8 ± 0.06 | 16.3 ± 0.40 | 0.32 ± 0.03 | 0.29 ± 0.03 | 66:34 |
| 225 °C | 31.7 ± 0.02 | 10.7 ± 0.14 | 0.21 ± 0.01 | 0.46 ± 0.03 | 34:66 |
| 325 °C | 29.8 ± 0.02 | 26.01 ± 0.14 | - | - | - |

The fitted CEMS spectra and the L-MOKE measurements were done on the annealed samples to further explore the temperature-dependent changes in magnetism. The resulting CEMS spectra and hysteresis loops are presented in Fig. 5 (a, b) and (c, d). Thermal annealing reveals a systematic change in the relative intensities of the CEMS peaks, indicating that the structure

of the two interfaces changes with annealing. At 325 °C, the CEMS data shows a single peak. The best fit to the data is shown in the solid line. The parameters obtained from fitting CEMS data and the hyperfine field for the pristine and annealed samples are presented in Table. 1. The MOKE hysteresis loop after annealing at 225 °C is seen to have slightly more coercivity. After annealing at 325 °C, the loop is observed with negligible coercivity value. Also, the Moke signal decreases when the annealing temperature increases.

DISCUSSION

In the literature, the interfaces of Fe/Ag systems have been extensively studied using various techniques such as Rutherford backscattering (RBS) [33], CEMS [10,42], XRR, and in-situ scanning tunneling microscopy (STM) [43]. While these methods have provided valuable insights, each has notable limitations. For instance, in-situ STM captures intermediate deposition states but may not accurately represent the final interfacial structure after the complete layer formation. Similarly, RBS suffers from poor depth resolution, which limits its ability to resolve subtle interfacial features. On the other hand, XRR requires a sufficiently thick and uniform heavy atom layer to achieve adequate electron density contrast, limiting its application for thin or diffuse interfaces. In contrast to earlier works, the present work utilized the NRS technique in the presence of XSW, enabling precise, independent characterization of both Fe-on-Ag and Ag-on-Fe interfaces within a single sample only by varying the angle of incidence of X-ray.

The Fe fluorescence as a function of q around the first Bragg peak is shown in Fig. 2(a). The best fit to the XRF data for the as-prepared sample yields root mean square (rms) roughness values of 10 Å and 6 Å for the Fe-on-Ag and Ag-on-Fe interface, respectively. These results indicate that the Ag-on-Fe interface is smoother than the Fe-on-Ag interface. This asymmetry reflects differences in surface energy and atomic diffusivity during deposition. The origin of the two fluorescence peaks from a single Fe layer in the as-prepared state is explained by the contour plot of X-ray intensity within the multilayer [Fig. 3(a)], which is simulated using the parameters derived from the simultaneous fitting of the reflectivity and fluorescence [Fig. 2(a)]. The two peaks at $q_1=0.121 \text{ \AA}^{-1}$ and $q_2=0.135 \text{ \AA}^{-1}$ correspond to the Fe-on-Ag and Ag-on-Fe interfaces. Additionally, the CEMS spectrum of the as-prepared sample [Fig. 1(c)] reveals an overlap of a sharp sextet with a broad one. The sharp sextet represents the bulk Fe layer, while the broad sextet corresponds to the Fe atoms at the interfacial region, where neighboring Ag atoms reduce the hyperfine field. The spectrum was fitted with a distribution of hyperfine field plus a sharp sextet.

The hyperfine field of the sharp sextet is 32.8 T, which is slightly lower than that of α -Fe (33 T). This reduction can be attributed to some quenched disorder in the Fe layer or some diffusion of Ag atoms into the bulk Fe layer. The relative area of the sharp sextet to that of the broad sextet is 66:34. From this ratio, the width of the interfacial region can be approximated as follows: the total thickness of the Fe layer is 35 Å, with 34% residing in the interfacial region. Since there are two interfaces, 17% of the total Fe layer resides at one interface, equivalent to $0.17 \times 3.8 \sim 6.5$ Å of the Fe layer. Even if the Fe/Ag interfaces are perfectly sharp, two monolayers (3 Å) of Fe would have Ag atoms as nearest or next-nearest neighbors, resulting in a reduced hyperfine field. Therefore, the additional 3.5 Å (6.5 Å-3 Å) of the Fe layer has reduced the hyperfine field because of intermixing at the interface.

The sample was annealed at various temperatures to investigate the thermal effects on its magnetism and hyperfine field. The XRR fitting results reveal changes in the interface roughness of the W/Si multilayer due to annealing. The intensity of the first Bragg peak is primarily determined by the average interfaces of the W/Si multilayer. Notably, up to 225 °C, there is minimal change in interface roughness, suggesting that the interfaces remained stable. However, after annealing at 325 °C, the roughness increased from 6.5 Å to 8.5 Å. These results indicate that the W/Si multilayer remains exceptionally stable and maintains sufficient fluorescence yield around the Bragg peak up to 225 °C, ensuring reliable measurements within this thermal range.

It was observed that the hyperfine field profile at both the interface (^{57}Fe -on-Ag and Ag-on- ^{57}Fe) are not equal [Fig. 4(c)], which aligns well with the differences in interface roughness. The root mean square (rms) roughness of ^{57}Fe -on-Ag and Ag-on- ^{57}Fe interfaces in the as-prepared state was 10 Å and 6 Å, respectively.

As expected, thermal annealing induced significant changes in the Fe fluorescence due to interdiffusion at the interfaces [Fig. 3(d)]. After annealing at 325 °C, the two peaks strongly overlap and become a single broad peak. Complementary results from CEMS measurements, it is observed that, after annealing at 225 °C, the relative area of the sharp sextet to the broad sextet changes to 33:67 and at 325 °C shows a broad singlet, suggesting the total intermixing of Fe and Ag layer.

MOKE measurement in the as-prepared Fig. 1(e) and annealed state is also shown in Fig. 5 (c, d) revealing distinct changes in the magnetic behavior of the Fe layer. In the as-prepared state, the hysteresis loop exhibits finite coercivity, indicative of the ferromagnetic behavior of the bulk Fe layer. However, after annealing at 325 °C for one hour, the hysteresis loop shows

almost negligible coercivity, suggesting that the Fe layer has diffused into the Ag matrix. This behavior suggests that, with thermal annealing, the Fe layer diffuses inside the Ag layer, and after annealing at 325 °C for one hour, the trilayer becomes paramagnetic. This is understood in forming Fe nanoparticles in an Ag matrix, which exhibited a paramagnetic or superparamagnetic nature. This study highlights the capability of the technique to resolve two distinct interfaces (Ag-on-Fe and Fe-on-Ag) within a single sample simply by varying the incident angle. Furthermore, the weightage of the central ^{nat}Fe layer relative to the two interfaces is almost equal and negligible, making the experiment highly interface-selective and suitable for the precise characterization of interfacial properties.

CONCLUSIONS

This study demonstrates the utility of nuclear resonance scattering (NRS) under X-ray standing wave (XSW) conditions to achieve depth-resolved characterization of interfacial asymmetries in multilayer systems. By leveraging the W/Si multilayer to generate XSWs, the two interfaces (Fe-on-Ag and Ag-on-Fe) were independently analyzed within a single sample. The Fe-on-Ag interface was rough compared to the Ag-on-Fe interface, with RMS roughness values of 10 Å and 6 Å, respectively. These structural differences directly influence the magnetic properties, as evidenced by significant changes in fluorescence, hyperfine fields, and hysteresis behavior with thermal annealing. At elevated temperatures (325 °C), the Fe layer transitions to a paramagnetic state due to the formation of Fe nanoparticles within the Ag matrix.

The integration of NRS, XSW, and complementary techniques like XRF and CEMS highlights the potential of this approach to resolve interfacial properties with exceptional depth resolution and isotopic sensitivity. Such precise characterization is critical for understanding and optimizing multilayer systems' structural and magnetic behavior, paving the way for their application in advanced spintronic and nanotechnological devices.

ACKNOWLEDGMENTS

We gratefully acknowledge financial support from the Department of Science and Technology, Government of India (project CRG/2021/003094) and travel support within the framework of the India@DESY collaboration. One of the authors thanks DST for the INSPIRE fellow (IF210723)

REFERENCES

- [1] L. Vieux-Rochaz, R. Cuchet, M.H. Vaudaine, A new GMR sensor based on NiFe/Ag multilayers, *Sens Actuators A Phys* 81 (2000) 53–56. [https://doi.org/10.1016/S0924-4247\(99\)00115-6](https://doi.org/10.1016/S0924-4247(99)00115-6).
- [2] F. Spizzo, E. Angeli, D. Bisero, F. Ronconi, P. Vavassori, P. Allia, V. Selvaggini, M. Coisson, P. Tiberto, F. Vinai, GMR as a function of temperature in FeAg granular samples: The effect of magnetic interactions, *J Magn Magn Mater* 262 (2003) 88–91. [https://doi.org/10.1016/S0304-8853\(03\)00025-8](https://doi.org/10.1016/S0304-8853(03)00025-8).
- [3] M. Tamisari, F. Spizzo, M. Sacerdoti, G. Battaglin, F. Ronconi, Correlation between structural and giant magnetoresistance properties of Fe-Ag nanogranular films, *Journal of Nanoparticle Research* 13 (2011) 5203–5210. <https://doi.org/10.1007/s11051-011-0505-x>.
- [4] R. Hoffmann, D.E. Bürgler, P.J.A. Van Schendel, H.J. Hug, S. Martin, H.J. Güntherodt, Perpendicular magnetic domains of a thin Ag/Fe/Ag film observed by magnetic force microscopy at room temperature, *J Magn Magn Mater* 250 (2002) 32–38. [https://doi.org/10.1016/S0304-8853\(02\)00343-8](https://doi.org/10.1016/S0304-8853(02)00343-8).
- [5] C.H. Chang, K.P. Dou, Y.C. Chen, T.M. Hong, C.C. Kaun, Engineering the interlayer exchange coupling in magnetic trilayers, *Sci Rep* 5 (2015) 1–7. <https://doi.org/10.1038/srep16844>.
- [6] Y. Meng, J. Li, P.A. Glans, C.A. Jenkins, E. Arenholz, A. Tan, J. Gibbons, J.S. Park, C. Hwang, H.W. Zhao, Z.Q. Qiu, Magnetic interlayer coupling between antiferromagnetic CoO and ferromagnetic Fe across a Ag spacer layer in epitaxially grown CoO/Ag/Fe/Ag(001), *Phys Rev B Condens Matter Mater Phys* 85 (2012) 1–6. <https://doi.org/10.1103/PhysRevB.85.014425>.
- [7] J. Wu, J. Choi, A. Scholl, A. Doran, E. Arenholz, Y.Z. Wu, C. Won, C. Hwang, Z.Q. Qiu, Element-specific study of the anomalous magnetic interlayer coupling across NiO spacer layer in Co/NiO/Fe/Ag(001) using XMCD and XMLD, *Phys Rev B Condens Matter Mater Phys* 80 (2009) 4–7. <https://doi.org/10.1103/PhysRevB.80.012409>.
- [8] G. Sharma, R. Gupta, D. Kumar, A. Gupta, Anomalous evolution of interfaces in Fe/Ag magnetic multilayer, *J Phys D Appl Phys* 46 (2013). <https://doi.org/10.1088/0022-3727/46/50/505302>.
- [9] C. Rumbolz, W. Bolse, S. Kumar, R.S. Chauhan, D. Kabiraj, D.K. Avasthi, Smoothing of Fe/Au and Fe/Ag multilayers by swift heavy ion bombardment, *Nucl Instrum Methods Phys Res B* 245 (2006) 145–149. <https://doi.org/10.1016/j.nimb.2005.11.163>.
- [10] P.J. Schurer, Z. Celinski, B. Heinrich, Mössbauer investigation of the growth of the Fe multilayer in Fe(100)/Ag(100) structures, *Phys Rev B* 51 (1995) 2506–2514. <https://doi.org/10.1103/PhysRevB.51.2506>.
- [11] A. Gupta, D. Kumar, V. Phatak, Asymmetric diffusion at the interfaces in Fe/Si multilayers, *Phys Rev B* 81 (2010) 155402.
- [12] C.L. Chien, K.M. Unruh, Magnetic properties and hyperfine interactions in concentrated Fe-Ag alloys, *Phys Rev B* 28 (1983) 1214–1218. <https://doi.org/10.1103/PhysRevB.28.1214>.
- [13] A. Davies, J.A. Stroschio, D.T. Pierce, R.J. Celotta, Atomic-scale observations of alloying at the Cr-Fe(001) interface, *Phys Rev Lett* 76 (1996) 4175–4178. <https://doi.org/10.1103/PhysRevLett.76.4175>.
- [14] S. Singh, A.G. Khanderao, M. Gupta, I. Sergeev, H.C. Wille, K. Schlage, M. Herlitschke, D. Kumar, Origin of exchange bias in [Co/Pt]ML/Fe multilayers with orthogonal magnetic anisotropies, *Phys Rev B* 108 (2023). <https://doi.org/10.1103/PhysRevB.108.075414>.

- [15] D. Kumar, A. Gupta, Effects of interface roughness on interlayer coupling in Fe/Cr/Fe structure, in: *Hyperfine Interact*, 2005: pp. 165–172. <https://doi.org/10.1007/s10751-005-9160-x>.
- [16] R. Rüffer, Nuclear resonance scattering, *C R Phys* 9 (2008) 595–607. <https://doi.org/10.1016/j.crhy.2007.06.003>.
- [17] A. Gupta, M. Gupta, S. Chakravarty, R. Rüffer, H.C. Wille, O. Leupold, Fe diffusion in amorphous and nanocrystalline alloys studied using nuclear resonance reflectivity, *Phys Rev B Condens Matter Mater Phys* 72 (2005) 1–8. <https://doi.org/10.1103/PhysRevB.72.014207>.
- [18] A. Gupta, D. Kumar, M.A. Andreeva, A.D. Gribova, R. Rüffer, Depth resolved hyperfine interactions with standing waves in [W/Si] 10/Si/Ag/57Fe/Ag/Si multilayer, *J Phys Conf Ser* 217 (2010). <https://doi.org/10.1088/1742-6596/217/1/012116>.
- [19] V.G. Kohn, A.I. Chumakov, R. Rüffer, Combined nuclear-molecular resonance inelastic scattering of X rays, *Phys Rev Lett* 92 (2004) 1–4. <https://doi.org/10.1103/PhysRevLett.92.243001>.
- [20] M.A. Andreeva, R.A. Baulin, A.I. Chumakov, R. Rüffer, G. V. Smirnov, Y.A. Babanov, D.I. Devyaterikov, M.A. Milyaev, D.A. Ponomarev, L.N. Romashev, V. V. Ustinov, Nuclear resonance reflectivity from a [57Fe/Cr]30 multilayer with the Synchrotron Mössbauer Source, *J Synchrotron Radiat* 25 (2018) 473–483. <https://doi.org/10.1107/S1600577517017192>.
- [21] A. Gupta, D. Kumar, V. Phatak, Asymmetric diffusion at the interfaces in Fe/Si multilayers, *Phys Rev B* 81 (2010) 155402.
- [22] M.S. Jamal, P. Gupta, R. Raj, M. Gupta, V.R. Reddy, D. Kumar, Structural and magnetic asymmetry at the interfaces of MgO/FeCoB/MgO trilayer: Precise study under x-ray standing wave conditions, *J Appl Phys* 131 (2022). <https://doi.org/10.1063/5.0092977>.
- [23] S. Kaushik, R. Raj, I. Sergeev, P. Gupta, V.R. Reddy, D. Kumar, Depth Resolved Magnetic Studies of Fe/57Fe/C60 Bilayer Structure Under X-Ray Standing Wave Condition, *J Supercond Nov Magn* 37 (2024) 1181–1187. <https://doi.org/10.1007/s10948-024-06738-1>.
- [24] V.P. Londhe, A. Gupta, N. Ponpandian, D. Kumar, V.R. Reddy, TiO₂ as diffusion barrier at Co/Alq₃ interface studied by x-ray standing wave technique, *J Phys D Appl Phys* 51 (2018). <https://doi.org/10.1088/1361-6463/aabf7a>.
- [25] K.P. Mondal, S. Bera, A. Gupta, D. Kumar, A. Gome, V. Reddy Raghavendra, N. Ito, Y. Yamada-Takamura, P. Pandit, S. V. Roth, Effect of growth rate on quality of Alq₃ films and Co diffusion, *J Phys D Appl Phys* 54 (2021). <https://doi.org/10.1088/1361-6463/abd9eb>.
- [26] A. Gupta, D. Kumar, C. Meneghini, Interface structure in magnetic multilayers using x-ray standing waves, (2007) 1–6. <https://doi.org/10.1103/PhysRevB.75.064424>.
- [27] M.S. Jamal, S. Singh, A.S. Dev, N. Gupta, P. Gupta, M. Gupta, O. Leupold, I. Sergeev, V.R. Reddy, D. Kumar, Atypical magnetism in Pt/MgO/FeCoB/Pt waveguide structure by exchanging the order of MgO and FeCoB layers, *Acta Mater* 257 (2023). <https://doi.org/10.1016/j.actamat.2023.119150>.
- [28] S. Kaushik, A.G. Khanderao, M.S. Jamal, I. Sergeev, H.C. Wille, V.R. Reddy, D. Kumar, Study of obliquely deposited 57Fe layer on organic semiconductor (Alq₃); interface resolved magnetism under x-ray standing wave, *Hyperfine Interact* 242 (2021) 1–9. <https://doi.org/10.1007/s10751-021-01756-0>.
- [29] A.G. Khanderao, I. Sergeev, H.C. Wille, D. Kumar, Interface resolved magnetism at metal-organic (Fe/Alq₃) interfaces under x-ray standing wave condition, *Appl Phys Lett* 116 (2020). <https://doi.org/10.1063/1.5135361>.

- [30] A. Gupta, D. Kumar, C. Meneghini, J. Zegenhagen, Depth resolved x-ray absorption fine structure study in magnetic multilayers using x-ray standing waves, *J Appl Phys* 101 (2007). <https://doi.org/10.1063/1.2711698>.
- [31] A.G. Khanderao, S. Kaushik, A.S. Dev, V.R. Reddy, I. Sergueev, H.C. Wille, P. Pandit, S. V. Roth, D. Kumar, Interface magnetism in Fe/Alq₃ bilayer; interface resolved nuclear resonance scattering studies, *J Magn Magn Mater* 560 (2022) 169663. <https://doi.org/10.1016/j.jmmm.2022.169663>.
- [32] M.A. Andreeva, B. Lindgren, Standing waves and reflectivity from an ultrathin layer, *JETP Lett* 76 (2002) 704–706. <https://doi.org/10.1134/1.1556209>.
- [33] R. Gupta, M. Weisheit, H.U. Krebs, P. Schaaf, Interface structure of Fe/Ag multilayers prepared by pulsed laser deposition, *Phys Rev B Condens Matter Mater Phys* 67 (2003) 1–7. <https://doi.org/10.1103/PhysRevB.67.075402>.
- [34] M.S. Jamal, P. Gupta, I. Sergeev, O. Leupold, D. Kumar, Interface-resolved study of magnetism in MgO/FeCoB/MgO trilayers using x-ray standing wave techniques, *Phys Rev B* 107 (2023) 1–11. <https://doi.org/10.1103/PhysRevB.107.075416>.
- [35] M.A. Andreeva, Surface and interface investigations by nuclear resonant scattering with standing waves, *Hyperfine Interact* 156–157 (2004) 595–606. <https://doi.org/10.1023/b:hype.0000043281.88327.54>.
- [36] S.K. Ghose, B.N. Dev, A. Gupta, Resonance enhancement of x-rays and fluorescence yield from marker layers in thin films, *Phys Rev B Condens Matter Mater Phys* 64 (2001) 2334031–2334034. <https://doi.org/10.1103/physrevb.64.233403>.
- [37] S.K. Kim, J.B. Kortright, Modified magnetism at a buried Co/Pd interface resolved with X-ray standing waves, *Phys Rev Lett* 86 (2001) 1347–1350. <https://doi.org/10.1103/PhysRevLett.86.1347>.
- [38] A. Gupta, P. Rajput, A. Saraiya, V.R. Reddy, M. Gupta, S. Bernstorff, H. Amenitsch, Depth profiling of marker layers using x-ray waveguide structures, *Phys Rev B Condens Matter Mater Phys* 72 (2005). <https://doi.org/10.1103/PhysRevB.72.075436>.
- [39] M.A. Andreeva, B. Lindgren, Nuclear resonant spectroscopy at Bragg reflections from periodic multilayers: Basic effects and applications, *Phys Rev B Condens Matter Mater Phys* 72 (2005) 1–22. <https://doi.org/10.1103/PhysRevB.72.125422>.
- [40] A. Glavic, M. Björck, GenX 3: The latest generation of an established tool, *J Appl Crystallogr* 55 (2022) 1063–1071. <https://doi.org/10.1107/S1600576722006653>.
- [41] M.A. Andreeva, Nuclear resonant reflectivity data evaluation with the "rEFTIM" program, *Hyperfine Interact* 185 (2008) 17–21. <https://doi.org/10.1007/s10751-008-9806-6>.
- [42] G. Sharma, R. Gupta, A. Gupta, Study of interfacial modification in Fe/Ag multilayer with thermal annealing using X ray standing wave, *AIP Conf Proc* 1349 (2011) 661–662. <https://doi.org/10.1063/1.3606031>.
- [43] Y.J. Choi, I.C. Jeong, J. Park, S. Kahng, J. Lee, Y. Kuk, Surface alloy formation of Fe on Cr "100 ... studied by scanning tunneling microscopy, 59 (1999) 918–922.